A thermomechanical model for argillaceous hard soils–weak rocks: application to THM simulation of deep excavations in claystone

SAEED TOURCHI*, MIGUEL A. MÁNICA†, ANTONIO GENS‡, JEAN VAUNAT‡, MINH-NGOC VU§ and GILLES ARMAND‖

The paper presents the enhancement of an existing constitutive model for argillaceous hard soils–weak rocks to incorporate non-isothermal conditions, to be used in coupled thermo-hydro-mechanical (THM) simulations of underground excavations subjected to temperature variations within the context of deep geological nuclear waste disposal. The proposed thermo-elastoplastic extension accounts for the effect of temperature on the yield and plastic potential functions and on the elastic stiffness. The resulting model is validated through the simulation of relevant non-isothermal laboratory tests reported in the literature. The model is then applied to the coupled THM simulation of an in situ heating test conducted at the Meuse/Haute-Marne underground research laboratory in Bure, France, excavated in the Callovo-Oxfordian claystone. Results show that the incorporation of thermal effects into the constitutive description of the host rock plays a significant role in the behaviour of the excavation when subjected to thermal loading, particularly in the evolution of the excavation fractured zone.

KEYWORDS: claystone; constitutive modelling; elastoplasticity; numerical modelling; pore pressures; thermal behaviour; THM analyses; time dependence; underground excavations

INTRODUCTION

This contribution addresses the thermo-hydro-mechanical (THM) modelling of indurated argillaceous materials – that is, geological materials where clay minerals predominate and bonding is significant. They frequently occupy a transition zone where they can be classified either as hard soils or weak rocks, and they are widely distributed in nature, representing up to 50% of the global sedimentary rock mass (Gens, 2013). Recent interest in these materials arises from the fact that they are currently being considered as potential host media for high- and intermediate-level long-lived nuclear waste. They provide advantageous features such as low permeability, a degree of self-healing capacity and substantial retardation properties for solute transport (Gens, 2013; Armand *et al.*, 2017). However, they are sensitive to chemical changes, and because of their relatively low strength, excavations often require support (Gens *et al.*, 2007). In situ observations have also shown that excavation operations induce damage in these materials in the form of fracture networks (see, e.g. Armand *et al.*, 2014). The zone containing these fractures is usually known as the excavation fractured zone, and it plays a major role in the hydromechanical behaviour of underground excavations (Mánica *et al.*, 2022a, 2022b).

Given the exothermic nature of radioactive waste, temperature increases will take place in the host rock around the disposal cells. Therefore, the potential effects of this thermal loading, particularly on the fractured zone, are important aspects to consider in the performance assessment of deep geological repositories. The host rock, where the exothermic waste canisters will be placed, will be exposed to various coupled mechanical, hydraulic and thermal phenomena that can affect the near-field behaviour of excavations and the evolution of the fractured zone. Therefore, proper understanding and modelling of nuclear waste repositories require the incorporation of those phenomena in the constitutive description of the host rock.

Several thermomechanical models that can reproduce most of the observed behaviour of saturated clays at elevated temperatures have been developed by several researchers. Hueckel & Borsetto (1990) developed one of the first models by extending the well-known modified Cam Clay (MCC) model to consider thermo-elastoplastic behaviour. The proposed model accounts for the shrinking of the elastic domain during heating (thermal softening) and expansion during cooling when the stress state is within the yield surface. Adopting similar assumptions, subsequent models accounting for temperature effects are based on the same principle (Robinet *et al.*, 1996; Modaressi & Laloui, 1997; Cui *et al.*, 2000; Graham *et al.*, 2001; Abuel-Naga *et al.*, 2009; Laloui & François, 2009; Yao & Zhou, 2013; Di Donna & Laloui, 2015; Hamidi *et al.*, 2015; Tourchi & Hamidi, 2015; Hamidi *et al.*, 2017; Hamidi & Tourchi, 2018). Furthermore, the concept of bounding surface plasticity has also been extended to improve modelling of cyclic behaviour at various temperatures and volume changes under thermal loading at intermediate and highly overconsolidated states (Modaressi & Laloui, 1997; Laloui & Cekerevac, 2008; Laloui & François, 2009; Di Donna & Laloui, 2015; Zhou *et al.*, 2017; Cheng *et al.*, 2020; Golchin *et al.*, 2022).

Many of the thermomechanical models mentioned above are formulated within the framework of critical state soil

mechanics, assuming the yield function of the MCC model, in which thermo-plastic behaviour is incorporated using a temperature-dependent yield pressure. The latter is particularly suitable for normally consolidated (or lightly over-consolidated) soft clays, where their behaviour is controlled, to a large extent, by a volumetric yielding mechanism. However, this is not necessarily the case for indurated argillaceous materials, where strong post-sedimentation diagenetic bonds make the mobilisation of the shear resistance more likely in typical engineering applications, including deep tunnelling. Therefore, from a practical standpoint, a Mohr–Coulomb type failure criterion can be deemed adequate for characterising the behaviour of the stiff clayey materials considered as possible host mediums for deep geological disposal (Mánica *et al.*, 2017). Nevertheless, as shown by experimental evidence (e.g. De Bruyn & Thimus, 1996; Zhang *et al.*, 2007; Menaceur *et al.*, 2015; Liu *et al.*, 2019), strength and stiffness parameters are affected by temperature changes that might affect the behaviour of excavations.

In this context, the aim of the present work is to provide a thermomechanical model for argillaceous rocks, with emphasis on the deviatoric yielding mechanism, to be used in coupled thermo-hydro-mechanical (THM) simulations of underground excavations subjected to temperature variations. In particular, the work involves the extension of the constitutive model from Mánica *et al.* (2017), hereafter called the reference model, to non-isothermal conditions. The reference model uses a Mohr–Coulomb yield criterion and incorporates a number of features that are considered relevant for the satisfactory description of indurated clayey materials, such as strength and stiffness anisotropy, non-linear isotropic hardening/softening, time-dependent deformations and the evolution of permeability with the accumulation of irreversible strains. The proposed thermo-elastoplastic extension accounts for the effect of temperature on the yield and plastic potential functions as well as on the elastic stiffness. The resulting model is validated through the simulation of relevant non-isothermal laboratory test results reported in the literature. The model is then applied to the coupled THM modelling of an in situ heating test (Bumbieler *et al.*, 2021) carried out at the Meuse/Haute-Marne (MHM) underground research laboratory (URL), excavated in the Callovo Oxfordian (COx) claystone. This in situ experiment has already been simulated by Tourchi *et al.* (2021), using the isothermal version of the reference model. Although the previous results were satisfactory, it is shown here that the incorporation of thermal effects into the constitutive description of the host rock plays a significant role in the behaviour of the excavation when subjected to thermal loading, particularly in the evolution of the fractured zone.

THERMOMECHANICAL BEHAVIOUR OF ARGILLACEOUS ROCKS

A large amount of experimental data exists on the thermomechanical behaviour of clayey soils. In general, heating saturated clays under drained conditions induces strength and volume changes that depend on the stress history. Temperature-induced volume changes tend to be contractive and irreversible for normally consolidated clays, whereas expansive and reversible deformations occur for highly overconsolidated clays (Campanella & Mitchell, 1968; Plum & Esrig, 1969; Baldi *et al.*, 1988; Hueckel & Borsetto, 1990; Sultan *et al.*, 2002; Cekerevac & Laloui, 2004; Abuel-Naga *et al.*, 2006; Tsutsumi & Tanaka, 2012; Di Donna & Laloui, 2015; Shetty *et al.*, 2019). However, experimental data on the thermomechanical behaviour of

argillaceous rocks are still scarce in the scientific literature (Zhang *et al.*, 2007, 2014; Monfared *et al.*, 2012; Menaceur *et al.*, 2015; Liu *et al.*, 2019). In general, two main phenomena regarding the thermo-mechanical behaviour of argillaceous rocks appear of major importance: (*a*) continuous variation of mechanical properties (e.g. strength and stiffness parameters) with temperature, with a transition to a more ductile behaviour at elevated temperatures and (*b*) temperature-induced reversible expansive strains, followed, at some threshold temperature value, by irreversible contractive strains. These phenomena are further discussed in the following sections.

Temperature-induced changes in mechanical properties

De Bruyn & Thimus (1996) performed a number of isotropically consolidated undrained (CIU) triaxial tests at different temperatures on Boom clay samples (Fig. 1(a)), a Tertiary plastic clay of modest cementation and relatively low strength. They show that heating up to about 80°C led to a considerable loss of the shear strength of the material. With respect to the thermal behaviour of stiffer argillaceous rocks, Zhang *et al.* (2007) observed in CIU triaxial tests on Opalinus clay samples that the peak deviatoric stress and the stiffness reduce with increasing temperature, showing an increasingly ductile behaviour (Fig. 1(b)). Menaceur *et al.*
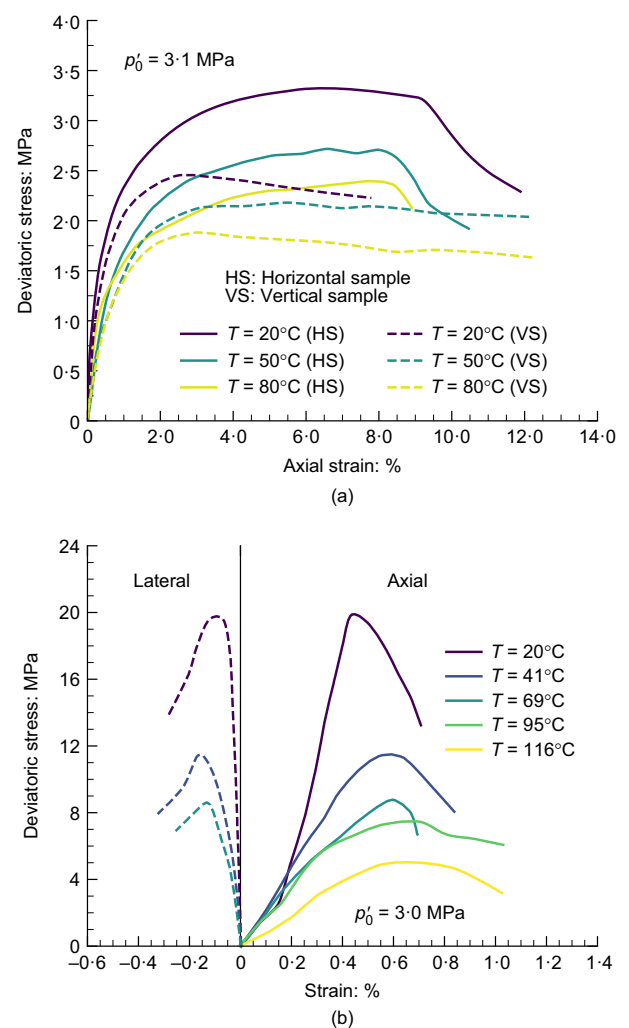

Fig. 1. Results of CIU triaxial test at different temperatures on (a) Boom clay (De Bruyn & Thimus, 1996) and (b) Opalinus clay (Zhang *et al.*, 2007). A full-colour version of this figure can be found on the ICE Virtual Library (www.icevirtuallibrary.com)

(2015) confirmed these observations on COx claystone under drained conditions (Fig. 2). More recently, Liu *et al.* (2019) conducted a series of drained lateral decompression tests, at constant mean stress, on COx samples (Fig. 3). Again, a reduction of the strength is observed as temperature increases, confirming the temperature-driven strength evolution.

Figure 4 summarises the test results from Figs 1–3 in terms of the peak strength as a function of temperature. It can be observed that the peak deviatoric stress generally reduces monotonically with temperature, showing a similar trend in all test series. Of course, the actual peak values depend on the material, reflecting their different origin, diagenesis and subsequent geological history, and on the loading path imposed by the tests performed. Boom clay samples show strengths about half an order of magnitude lower than COx and Opalinus clay samples. Nevertheless, results can be normalised with respect to the strength at a given reference temperature T_0. Fig. 5 shows this normalisation in terms of $q_{peak}(T)/q_{peak}(T_0)$ plotted against T/T_0, where $q_{peak}(T)$ is the peak deviatoric stress at a given temperature T and $q_{peak}(T_0)$

Fig. 4. **Evolution of peak strength with temperature for (a) Boom clay and (b) Opalinus clay and COx claystone samples**
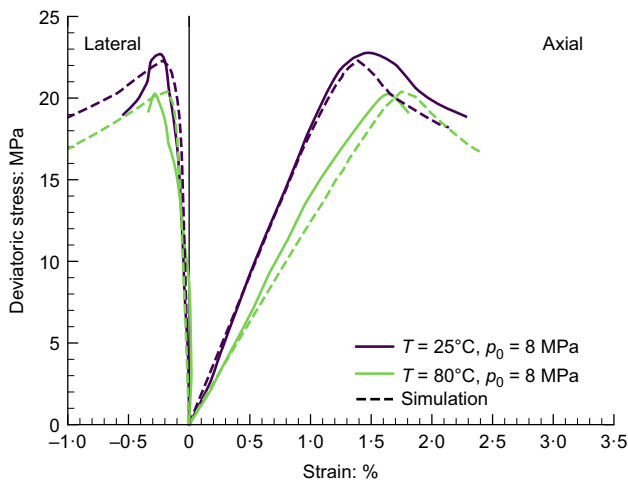

Fig. 2. **Results of drained hollow cylinder triaxial tests (Menaceur *et al.*, 2015) on COx samples at different temperatures and simulation results**

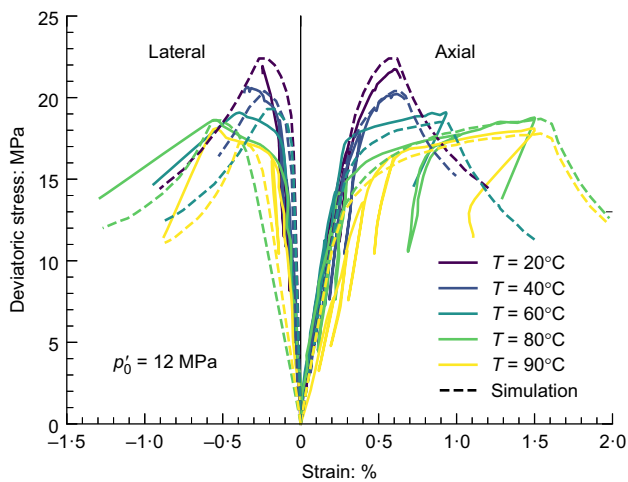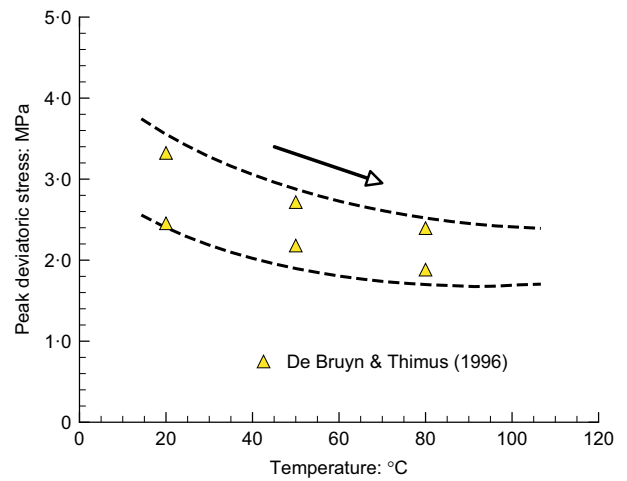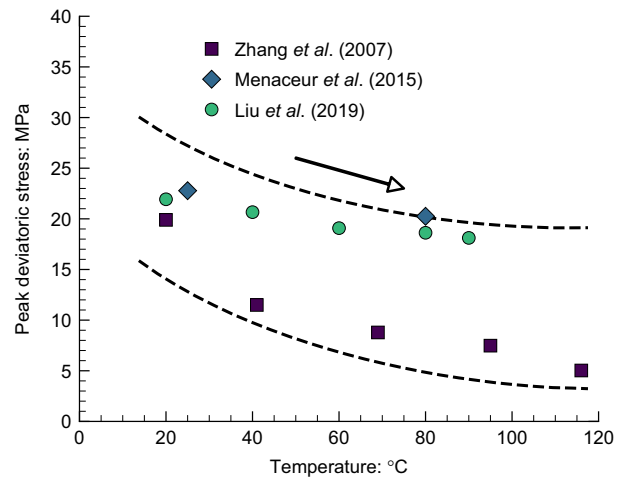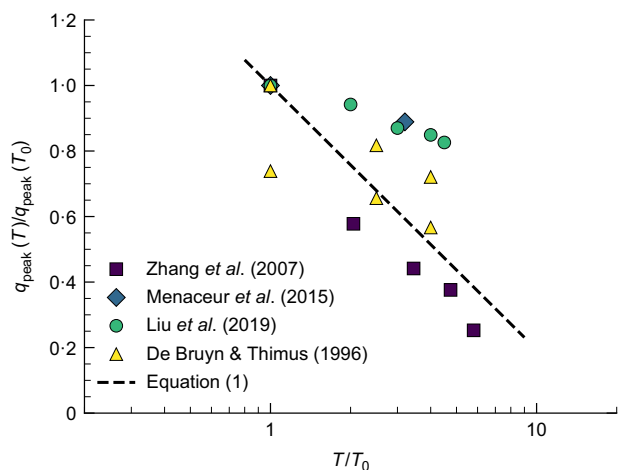Fig. 5. **Normalised evolution of peak strength with temperature**

Fig. 3. **Results of drained lateral decompression tests (Liu *et al.*, 2019) on COx samples at different temperatures and simulation results. A full-colour version of this figure can be found on the ICE Virtual Library (www.icevirtuallibrary.com)**

is the peak deviatoric stress at the reference temperature T_0, assumed here equal to the smallest testing temperature. Although some scatter is observed, from a practical stand-point, the dependence of the strength on temperature can be characterised through the following expression:

$$q_{\text{peak}}(T) = q_{\text{peak}}(T_0)\left[1 - \mu_q \ln(T/T_0)\right] \tag{1}$$

where μ_q is a parameter controlling the rate of strength reduction. Although equation (1) only refers to the variation of the peak deviatoric strength with temperature for specific conditions and stress paths, it can serve as the basis for defining the evolution laws of the yield envelope as a function of temperature for this indurated clayey materials, as is done in a later section 'Thermo-plastic components'.

As already mentioned, the stiffness also tends to reduce with temperature. For instance, Fig. 6 shows the variation of Young's modulus E from the tests shown in Fig. 5 in terms of $E(T)/E(T_0)$ plotted against T/T_0, where $E(T_0)$ is Young's modulus at the reference temperature T_0 and $E(T)$ is the Young's modulus at a given temperature T. A similar behaviour is observed as in Fig. 5 and, therefore, the variation of the E with temperature can be approximated with a similar relationship as equation (1)

$$E(T) = E(T_0)[1 - \mu_E \ln(T/T_0)] \tag{2}$$

where μ_E controls the rate of reduction of Young's modulus with temperature. Equations (1) and (2) are the basis for the proposed thermal extension of the reference model, described in the later section 'Thermomechanical extension'.

Temperature-induced volumetric strains

Thermal volume changes in clays subjected to a temperature increase under constant stress depend on the degree of consolidation; thermo-elastic expansion and thermo-plastic contraction are observed for overconsolidated and normally consolidated clays, respectively. However, as already mentioned, information on this matter is scarce for argillaceous indurated materials, such as those addressed in this work. For instance, in the case of COx claystone, Mohajerani *et al.* (2014) and Menaceur *et al.* (2015) first reported a contracting thermo-plastic behaviour similar to that of normally consolidated clays. However, Zhang *et al.* (2017) later observed a thermal expansion behaviour in COx and Opalinus clay samples under different confinement pressures and different heating and cooling paths. More recent testing (Belmokhtar *et al.*, 2017) also shows that indurated clayey materials first exhibit an elastic (reversible) thermal expansion, followed by a transition to a plastic thermal compression at some threshold temperature. The latter observations suggest that temperature might also affect the volumetric yielding mechanism of these materials, and this behaviour might be incorporated through a volumetric
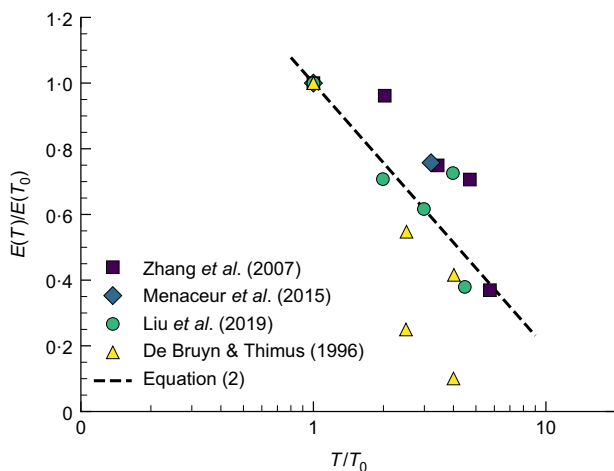

Fig. 6. Normalised evolution of Young's modulus with temperature

yielding cap that depends on temperature. Nevertheless, the present work focuses on the deviatoric yielding mechanism, and this expansion–contraction transition is not addressed here.

THERMOMECHANICAL CONSTITUTIVE MODEL
Isothermal reference model (Mánica et al., 2017)

The reference model is implemented in terms of effective stresses, adopting the following generalised expression accounting for the effects of potential desaturation

$$\boldsymbol{\sigma}' = \boldsymbol{\sigma} + S_{\text{e}}sB\boldsymbol{I} \tag{3}$$

where $\boldsymbol{\sigma}'$ is the total stress tensor; S_{e} is the effective degree of saturation; s is the suction; B is the Biot's coefficient; and $\boldsymbol{I}$ is the identity tensor. The equivalent degree of saturation is given by the following form of the van Genuchten (1980) expression

$$S_{\text{e}} = \frac{S_{\text{l}} - S_{\text{rl}}}{S_{\text{ls}} - S_{\text{rl}}} = \left[1 + \left(\frac{p_{\text{g}} - p_{\text{l}}}{P}\right)^{1/(1-\lambda_{\text{r}})}\right]^{\lambda_{\text{r}}} \tag{4}$$

where S_{l} is the degree of saturation; S_{lr} is the residual degree of saturation; S_{ls} is the degree of saturation in saturated conditions (normally 1); p_{g} and p_{l} are the gas and liquid pressures, respectively; λ_{r} is a shape function coefficient; and P can be interpreted as the air-entry pressure value. In the following, the term stress always denotes effective stress and, therefore, the prime is dropped. Also, following the soil mechanics sign convention, compressive stresses and strains are assumed positive.

The reference model comprises two main deformation mechanisms: (*a*) an instantaneous one related to the immediate deformations due to changes in effective stresses and (*b*) a time-dependent one occurring under constant effective stress. Note that the instantaneous response also includes deformations caused by changes in effective stresses associated with consolidation (i.e. hydromechanical coupling). The instantaneous response is described within the framework of elastoplasticity, while for the time-dependent response, an additional deformation mechanism is considered following the plasticity–creep partition approach (Chaboche, 2008). Therefore, the strain decomposition assumed reads as follows

$$d\varepsilon = d\varepsilon^{\text{ep}} + d\varepsilon^{\text{vp}} = d\varepsilon^{\text{ep}} + d\dot{\boldsymbol{\varepsilon}}^{\text{vp}} \tag{5}$$

where $d\varepsilon$ is the total strain increment; $d\varepsilon^{\text{ep}}$ is the elastoplastic strain increment, related to the instantaneous response; $d\varepsilon^{\text{vp}}$ is the viscoplastic strain increment, related to the time-dependent response; dt is the time increment; and $\dot{\boldsymbol{\varepsilon}}^{\text{vp}}$ is the viscoplastic strain rate tensor.

Under low deviatoric stresses, the response is linear elastic and characterised by a transversely isotropic (or cross-anisotropic) form of Hooke's law (see Wittke (1990)). For higher deviatoric stress, plastic deformations develop on reaching the yield surface, characterised by the Mohr–Coulomb criterion

$$f = \left(\cos\theta + \frac{1}{\sqrt{3}}\sin\theta\sin\phi_{\text{mob}}\right)J$$
$$- \sin\phi_{\text{mob}}(c_{\text{mob}}\cot\phi_{\text{mob}} + p) \tag{6}$$

where ϕ_{mob} is the mobilised friction angle; c_{mob} is the mobilised cohesion; and the remaining variables are stress invariants with their usual definition

$$p = \frac{1}{3}\,\text{tr}\boldsymbol{\sigma} \tag{7}$$

$$J = \left(\frac{1}{2}\, \mathrm{tr}\mathbf{s}^2\right)^{1/2} \tag{8}$$

$$\theta = -\frac{1}{3} \sin^{-1}\left(\frac{3\sqrt{3}\det\mathbf{s}}{2J^3}\right) \tag{9}$$

where $\mathbf{s} = \boldsymbol{\sigma} - p\mathbf{I}$ is the deviatoric stress tensor.

Hardening/softening is accounted for through the evolution of the strength parameters. The friction angle varies in a piecewise manner as follows

$$\phi_{\mathrm{mob}} = \begin{cases} \phi_{\mathrm{ini}} + \dfrac{\varepsilon_{\mathrm{eq}}^{\mathrm{p}}}{a_{\mathrm{hard}} - \dfrac{\varepsilon_{\mathrm{eq}}^{\mathrm{p}}\left\{a_{\mathrm{hard}} - \left[\xi_1/\left(\phi_{\mathrm{peak}} - \phi_{\mathrm{ini}}\right)\right]\right\}}{\xi_1}} & \text{if } \varepsilon_{\mathrm{eq}}^{\mathrm{h}} \leq \xi_1 \\[3em] \phi_{\mathrm{peak}} & \text{if } \xi_1 < \varepsilon_{\mathrm{eq}}^{\mathrm{p}} \leq \xi_2 \\[2em] \phi_{\mathrm{peak}} - \dfrac{\varepsilon_{\mathrm{eq}}^{\mathrm{p}} - \xi_2}{a_{\mathrm{soft}} - \dfrac{\left\{a_{\mathrm{soft}} - \left[(\xi_3 - \xi_2)/\left(\phi_{\mathrm{peak}} - \phi_{\mathrm{res}}\right)\right]\right\}\left(\varepsilon_{\mathrm{eq}}^{\mathrm{p}} - \xi_2\right)}{\xi_3 - \xi_2}} & \text{if } \xi_2 < \varepsilon_{\mathrm{eq}}^{\mathrm{p}} \leq \xi_3 \\[3em] \phi_{\mathrm{res}} & \text{if } \varepsilon_{\mathrm{eq}}^{\mathrm{p}} > \xi_3 \end{cases} \tag{10}$$

where ϕ_{ini} is the initial friction angle; ϕ_{peak} is the peak friction angle; ϕ_{res} is the residual friction angle; $\varepsilon_{\mathrm{eq}}^{\mathrm{p}}$ is the state variable controlling hardening/softening (equation (11)); ξ_1 is the value of $\varepsilon_{\mathrm{eq}}^{\mathrm{p}}$ at peak strength; ξ_2 is the value of $\varepsilon_{\mathrm{eq}}^{\mathrm{p}}$ at which softening begins; ξ_3 is the value of $\varepsilon_{\mathrm{eq}}^{\mathrm{p}}$ at which the residual strength is reached; a_{hard} is a parameter controlling the curvature of the function in the hardening branch; and a_{soft} is a parameter controlling the curvature of the function in the softening branch.

$$\varepsilon_{\mathrm{eq}}^{\mathrm{p}} = \left(\frac{2}{3}\, \boldsymbol{\varepsilon}^{\mathrm{p}} : \boldsymbol{\varepsilon}^{\mathrm{p}}\right)^{1/2} \tag{11}$$

where $\boldsymbol{\varepsilon}^{\mathrm{p}}$ is the plastic strain tensor.

Cohesion evolves along with the friction angle, according to equation (12), to allow the rotation of the Mohr–Coulomb envelope during hardening/softening.

$$c_{\mathrm{mob}} = c_{\mathrm{peak}} \cot\phi_{\mathrm{peak}} \tan\phi_{\mathrm{mob}} \tag{12}$$

where c_{peak} is the peak cohesion.

The model also accounts for strength cross-anisotropy (or transverse isotropy) through a non-uniform scaling of the stress tensor (Mánica et al., 2016). The latter approach is incorporated by replacing p, J and θ, used to evaluate the yield condition (equation (6)), by p^{ani}, J^{ani} and θ^{ani}, respectively. These are invariants, with the same definition as in equations (7)–(9), but computed from the anisotropic stress tensor $\boldsymbol{\sigma}^{\mathrm{ani}}$, defined as

$$\boldsymbol{\sigma}^{\mathrm{ani}} = \begin{bmatrix} \dfrac{\sigma_{11}^r}{c_{\mathrm{N}}} & c_{\mathrm{S}}\sigma_{12}^r & \sigma_{13}^r \\[1em] c_{\mathrm{S}}\sigma_{12}^r & c_{\mathrm{N}}\sigma_{22}^r & c_{\mathrm{S}}\sigma_{23}^r \\[1em] \sigma_{13}^r & c_{\mathrm{S}}\sigma_{23}^r & \dfrac{\sigma_{33}^r}{c_{\mathrm{N}}} \end{bmatrix} \tag{13}$$

where c_{N} and c_{S} are the normal and shear scaling factors, respectively, and σ_{ii}^r are the components of $\boldsymbol{\sigma}^r$. The latter corresponds to the stress tensor $\boldsymbol{\sigma}$, but oriented in such a way that direction $t2$ is normal to the isotropic plane (i.e. normal to bedding in these sedimentary materials) by way of the usual rotation transformation. In this way, the yield surface is indirectly modified to account for cross-anisotropy. Further

details on this approach, and on the physical meaning of the anisotropy parameters, are provided in Mánica et al. (2016).

Regarding the direction of plastic flow, a non-associated flow rule is adopted. Rather than deriving a specific function for the plastic potential, the flow rule is directly obtained from the yield criterion in the following way

$$\frac{\partial g}{\partial \boldsymbol{\sigma}} = \omega \frac{\partial f}{\partial p}\frac{\partial p}{\partial \boldsymbol{\sigma}} + \frac{\partial f}{\partial J}\frac{\partial J}{\partial \boldsymbol{\sigma}} + \frac{\partial f}{\partial \theta}\frac{\partial \theta}{\partial \boldsymbol{\sigma}} \tag{14}$$

where g is the plastic potential function, and ω is a constant controlling the volumetric component of plastic deformations.

With $\omega = 1$, an associated flow rule is recovered, while with $\omega = 0$, no volumetric plastic strains occur. An adequate value for geomaterials usually lies between these limits. However, it is important to notice that, owing to the non-uniform scaling approach to incorporate strength anisotropy, f is defined in terms of the anisotropic stress invariants p^{ani}, J^{ani} and θ^{ani}. Therefore, the flow rule is computed as follows

$$\frac{\partial g}{\partial \boldsymbol{\sigma}} = \omega \frac{\partial f}{\partial p^{\mathrm{ani}}}\frac{\partial p^{\mathrm{ani}}}{\partial \boldsymbol{\sigma}^{\mathrm{ani}}}\frac{\partial \boldsymbol{\sigma}^{\mathrm{ani}}}{\partial \boldsymbol{\sigma}} + \frac{\partial f}{\partial J^{\mathrm{ani}}}\frac{\partial J^{\mathrm{ani}}}{\partial \boldsymbol{\sigma}^{\mathrm{ani}}}\frac{\partial \boldsymbol{\sigma}^{\mathrm{ani}}}{\partial \boldsymbol{\sigma}}$$
$$+ \frac{\partial f}{\partial \theta^{\mathrm{ani}}}\frac{\partial \theta^{\mathrm{m}}}{\partial \boldsymbol{\sigma}^{\mathrm{ani}}}\frac{\partial \boldsymbol{\sigma}^{\mathrm{ani}}}{\partial \boldsymbol{\sigma}} \tag{15}$$

where $\partial \boldsymbol{\sigma}^{\mathrm{ani}}/\partial \boldsymbol{\sigma}$ is a Jacobian matrix containing the partial derivatives of the anisotropic stress components with respect to the global Cartesian stresses. In this way, the standard derivatives of the stress invariants are unchanged. $\partial \boldsymbol{\sigma}^{\mathrm{ani}}/\partial \boldsymbol{\sigma}$ depends on the scaling factors C_{N} and C_{S} and on the orientation of the isotropic plane, and its definition can be found in Mánica et al. (2016). The same approach can be applied to compute the gradient of the yield function $\partial f/\partial \boldsymbol{\sigma}$, which is also required for the adopted implicit implementation.

For the characterisation of the time-dependent deformation component, the strain rate tensor is computed as

$$\dot{\boldsymbol{\varepsilon}}^{\mathrm{vp}} = \frac{2}{3}\frac{\dot{\varepsilon}^{\mathrm{vp}}}{q}\, \mathbf{s} \tag{16}$$

$$q = \left(\frac{3}{2}\, \mathbf{s} : \mathbf{s}\right)^{1/2} \tag{17}$$

$$\dot{\varepsilon}^{\mathrm{vp}} = \gamma\langle q - \sigma_{\mathrm{s}}\rangle^n \left(1 - \varepsilon_{\mathrm{eq}}^{\mathrm{vp}}\right)^m \tag{18}$$

where γ is a viscosity parameter; σ_{s} is a threshold from which viscoplastic strains are activated; $\langle \cdot \rangle$ are the Macaulay brackets; n and m are material constants; and $\varepsilon_{\mathrm{eq}}^{\mathrm{vp}}$ is the state variable of the time-dependent mechanism, given by

$$\varepsilon_{\mathrm{eq}}^{\mathrm{vp}} = \int_0^t \left(\frac{2}{3}\, \dot{\boldsymbol{\varepsilon}}^{\mathrm{vp}} : \dot{\boldsymbol{\varepsilon}}^{\mathrm{vp}}\right)^{1/2} \mathrm{d}t \tag{19}$$

Finally, the model assumes that the intrinsic permeability evolves with plastic deformations to account for the observed permeability increase with damage in the COx claystone (see, e.g. Armand *et al.*, 2014). The plastic multiplier λ is used to characterise the magnitude of the accumulated plastic deformations, and the intrinsic permeability tensor is defined by the following expression

$$\boldsymbol{k} = \begin{cases} k_0 \mathrm{e}^{\eta(\lambda-\lambda_{\mathrm{thr}})} & \text{if } \lambda > \lambda_{\mathrm{thr}} \\ k_0 & \text{if } \lambda \leq \lambda_{\mathrm{thr}} \end{cases} \tag{20}$$

where k_0 is the intrinsic permeability tensor of the intact rock; η is a constant that controls the rate of change; and λ_{thr} is a threshold value of λ from which permeability increases.

The model described has been successfully employed to simulate the behaviour of underground excavations in COx claystone (e.g. Gens *et al.*, 2017; Mánica *et al.*, 2017; Alonso *et al.*, 2021), and it was used to simulate the in situ heating tests addressed in this work (Tourchi *et al.*, 2021). Nevertheless, as shown in the earlier section on 'Thermomechanical behaviour of argillaceous rocks', accounting for thermal effects on the constitutive description of the COx claystone might play a significant role when the host rock is subjected to thermal loading.

Thermomechanical extension
Thermo-elastic deformations.   Assuming that the coefficient of thermal expansion is independent of stresses, the hypo-elastic (incrementally reversible) strain increment can be defined as the sum of the thermal and mechanical components

$$\mathrm{d}\varepsilon^{\mathrm{e}} = \mathrm{d}\varepsilon^{\mathrm{e},\sigma} + \frac{1}{3}\mathrm{d}\varepsilon_{\mathrm{v}}^{\mathrm{e},T}\boldsymbol{I} \tag{21}$$

where $\mathrm{d}\varepsilon^{\mathrm{e},\sigma}$ is the increment of elastic strains caused by changes in effective stresses and $\mathrm{d}\varepsilon_{\mathrm{v}}^{\mathrm{e},T}$ is the elastic volumetric strain increment caused by changes in temperature T. The latter can be defined as

$$\mathrm{d}\varepsilon_{\mathrm{v}}^{\mathrm{e},T} = 3\alpha_{\mathrm{s}}\mathrm{d}T \tag{22}$$

where α_{s} is the linear thermal expansion coefficient of the medium, which depends on the material mineralogy, temperature and pressure changes, although for practical purposes it can be assumed a constant.

Moreover, as discussed in the earlier section 'Temperature-induced changes in mechanical properties', the elastic stiffness, associated with $\mathrm{d}\varepsilon^{\mathrm{e},\sigma}$, is also affected by temperature. The latter is incorporated here through a dependence of the Young's modulus E on temperature according to equation (2). Since a transversely isotropic form of Hooke's low is being employed, equation (2) is applied to the elastic constants E_1 (Young's modulus parallel to the isotropic plane), E_2 (Young's modulus normal to the isotropic plane) and G_2 (shear modulus in planes normal to the isotropic plane), with the same μ_E value, while ν_1 (Poisson's ratio for the lateral strains due to loading parallel to the isotropic plane) and ν_2 (Poisson's ratio for the lateral strains due to loading normal to the isotropic plane) are assumed constant.

Thermo-plastic components.   Key thermal effects in argillaceous rocks, at least in the context of geological disposal of radioactive waste, are those leading to plastic deformations and, therefore, those affecting the fractured zone. As discussed in the earlier section 'Temperature-induced changes in mechanical properties', the strength of these indurated clayey materials depends on temperature, showing a monotonic reduction as temperature increases. This implies that larger plastic

deformations and a larger fractured zone can be expected under higher temperatures, such as those induced by exothermic nuclear waste. Following Hueckel & Borsetto (1990), this behaviour can be incorporated by assuming that the yield function depends also on temperature. As the adopted reference model is characterised by a Mohr–Coulomb yield function, strength dependence on temperature can be incorporated through parameters ϕ and c. Since this effect must be included in addition to the strength evolution due to mechanical loading (equations (10) and (12)), mobilised strength parameters must be a function of both plastic strains and temperature. In the case of the friction angle, equation (1) can be adopted to define ϕ_{ini}, ϕ_{peak}, ϕ_{res} as a function of temperature in the following way

$$\phi_{\mathrm{ini}}(T) = \phi_{\mathrm{ini}}^{T_0}\left[1 - \mu_\phi \ln(T/T_0)\right] \tag{23}$$

$$\phi_{\mathrm{peak}}(T) = \phi_{\mathrm{peak}}^{T_0}\left[1 - \mu_\phi \ln(T/T_0)\right] \tag{24}$$

$$\phi_{\mathrm{res}}(T) = \phi_{\mathrm{res}}^{T_0}\left[1 - \mu_\phi \ln(T/T_0)\right] \tag{25}$$

where $\phi_{\mathrm{ini}}^{T_0}$, $\phi_{\mathrm{peak}}^{T_0}$ and $\phi_{\mathrm{res}}^{T_0}$ are the initial, peak and residual friction angles, respectively, at the reference temperature T_0; and μ_ϕ is a parameter controlling the rate of change of the friction angle with temperature.

As in the case of mechanical loading, it is assumed that the Mohr–Coulomb envelope rotates around a fixed point and, therefore, the temperature-dependent mobilised cohesion can be defined as

$$c_{\mathrm{mob}}(T) = c_{\mathrm{peak}}^{T_0} \cot\phi_{\mathrm{peak}}^{T_0} \tan\phi_{\mathrm{mob}}(T) \tag{26}$$

where $c_{\mathrm{peak}}^{T_0}$ is the peak cohesion at the reference temperature T_0.

The incorporated dependence of the yield function with temperature requires the modification of the standard form of Prager's consistency condition. In the case of plastic loading, the latter reads

$$\mathrm{d}f = \frac{\partial f}{\partial\boldsymbol{\sigma}}\mathrm{d}\boldsymbol{\sigma} + \frac{\partial f}{\partial\phi_{\mathrm{mob}}}\mathrm{d}\phi_{\mathrm{mob}} = 0 \tag{27}$$

where

$$\mathrm{d}\phi_{\mathrm{mob}} = \frac{\partial\phi_{\mathrm{mob}}}{\partial\varepsilon_{\mathrm{eq}}^{\mathrm{p}}}\frac{\varepsilon_{\mathrm{eq}}^{\mathrm{p}}}{\partial\varepsilon^{\mathrm{p}}}\mathrm{d}\varepsilon^{\mathrm{p}} + \frac{\partial\phi_{\mathrm{mob}}}{\partial T}\mathrm{d}T \tag{28}$$

A term accounting for changes in the yield function due to changes in cohesion is omitted in equation (27) because it is assumed here that c_{mob} is a function of ϕ_{mob} (equation (26)). Therefore, these changes are already contained in the second term of equation (27). It is, of course, possible (and sometimes desired; see, e.g. Mánica *et al.* (2022a)) to define the cohesion independently from the friction angle. In the latter case, the additional term $(\partial f/\partial c_{\mathrm{mob}})\mathrm{d}c_{\mathrm{mob}}$ must be included in equation (27). The increment of plastic deformations $\mathrm{d}\varepsilon^{\mathrm{p}}$ is defined as

$$\mathrm{d}\varepsilon^{\mathrm{p}} = \mathrm{d}\lambda\frac{\partial g}{\partial\boldsymbol{\sigma}} \tag{29}$$

where λ is the plastic multiplier. By substituting equation (29) into equations (27) and (28), $\mathrm{d}\lambda$ can be defined as

$$\mathrm{d}\lambda = \frac{1}{H}\left(\frac{\partial f}{\partial\boldsymbol{\sigma}}\mathrm{d}\boldsymbol{\sigma} + \frac{\partial f}{\partial\phi_{\mathrm{mob}}}\frac{\partial\phi_{\mathrm{mob}}}{\partial T}\mathrm{d}T\right) \tag{30}$$

where

$$H = -\frac{\partial f}{\partial\phi_{\mathrm{mob}}}\frac{\partial\phi_{\mathrm{mob}}}{\partial\varepsilon_{\mathrm{eq}}^{\mathrm{p}}}\frac{\partial\varepsilon_{\mathrm{eq}}^{\mathrm{p}}}{\partial\varepsilon^{\mathrm{p}}}\frac{\partial g}{\partial\boldsymbol{\sigma}} \tag{31}$$

Therefore, plastic deformations are now also affected by the thermal variation of the strength parameters. Details on the loading/unloading conditions for thermomechanical paths, as well as the consequences of the thermal softening response for specific conditions, can be found in Hueckel & Borsetto (1990).

MODEL VALIDATION

In order to assess the described thermomechanical extension of the reference model, a number of laboratory tests on COx samples under different temperatures were simulated. Specifically, the hollow cylinder triaxial tests from Menaceur *et al.* (2015) and the lateral decompression tests from Liu *et al.* (2019), shown in Figs 2 and 3, were used in this modelling exercise. The parameters obtained, particularly those related to the thermal extension of the model, were later used in the simulation of the ALC1604 in situ heating test at the MHM URL. Simulations were performed from a constitutive stand-point, with a unit cube mesh and assuming a homogeneous stress/strain field. As reported in the experiments, drained conditions were considered. The latter hypothesis is much more likely to be fulfilled in the hollow cylinder triaxial tests from Menaceur *et al.* (2015) owing to the small drainage length. However, even if fully drained conditions did not occur in the experiments, the main interest here is in the relative changes between the tests at different temperatures. Therefore, so long as the initial conditions of all samples in each test series are similar, the simulations performed can still provide an assessment of the proposed thermal extension of the reference model. Both test series were carried out with the major principal stress normal to bedding and, therefore, anisotropy does not play a role in the results. The latter is only partially true since the difference between Young's moduli normal and parallel to bedding does affect the lateral elastic expansion in the case of the decompression test from Liu *et al.* (2019). Nevertheless, this effect is small and, therefore, no anisotropy in either stiffness or strength was incorporated in the simulation of the tests. The time-dependent component was also not included and, therefore, the viscosity parameter γ was assumed to be equal to zero. Although these features are not relevant in these simulations, they are relevant in the simulation of the in situ heating tests, described in the next section 'THM simulation of the ALC1604 in situ heating test'.

The simulated tests from Menaceur *et al.* (2015) were isotropically consolidated up to an effective mean stress of 8 MPa (close to in situ conditions) under 25°C. Then, in one of the tests, the temperature was increased up to 80°C. Both samples were then sheared under displacement control. Since the reference model does not include a volumetric yielding mechanism (cap), it is not necessary to reproduce the actual consolidation path followed and, therefore, the stress state and temperature before shearing were prescribed as initial conditions in the simulations. The parameters employed are summarised in Table 1. They were calibrated to achieve a reasonable agreement with experimental results. Since the tests were performed at a constant temperature, thermal parameters such as the linear thermal expansion coefficient α_s, the thermal conductivity k_T and the specific heat capacity c_s do not affect the results. They will be relevant, however, for the simulation of the in situ heating tests (see next section 'THM simulation of the ALC1604 in situ heating test'). In contrast, the thermal parameters μ_E and μ_ϕ, controlling the resulting stiffness and strength for different temperatures, were calibrated to reproduce the observed behaviour. Simulation results are compared against laboratory data in Fig. 2. It can be observed that the model was able to capture adequately the reduction of the stiffness and the strength when the temperature was increased from 25 to 80°C.

The tests from Liu *et al.* (2019) were consolidated isotropically to a mean effective stress of 12 MPa. The temperature was then increased at a rate of 20°C/h until reaching the target value for each test (20, 40, 60, 80 and 90°C). Again, the stress state and temperature were pre-scribed in the simulation as initial conditions before shearing. After reaching the target temperature, samples were then sheared by applying an axial displacement rate, resulting in a strain rate of 2×10^{-6} s^{-1}, while simultaneously reducing the confinement pressure to achieve a constant mean effective stress path. The parameters employed are also shown in Table 1, and the model results are compared against laboratory data in Fig. 3. Again, the model was able to capture satisfactorily the strength and stiffness reduction observed as the temperature was increased from 20 to 90°C.

THM SIMULATION OF THE ALC1604 IN SITU HEATING TEST

As previously mentioned, the ALC1604 in situ heating test, performed at the MHM URL, has already been simulated by Tourchi *et al.* (2021), using the reference model to characterise the host rock. Tourchi *et al.* (2021) reported two-dimensional (2D) and three-dimensional (3D) fully coupled THM analyses to explain the observed behaviour, particularly the near-field response of the host rock due to the increase in temperature. In general, simulations were able to reproduce satisfactorily in situ observations. A particular outcome of the analyses is that the fractured zone does not evolve significantly during the heating phase of the experiment; only a minor increase is observed as a result of creep and consolidation. However, the reference model assumes isothermal conditions and does not take into account the observed decrease of the strength and stiffness of the COx, and other indurated clayey materials, as temperature increases (see the earlier section 'Thermomechanical behaviour of argillaceous rocks'). Therefore, the analyses mentioned cannot assess the role of this feature of the clay rock in the behaviour of the excavation when subjected to thermal loading, particularly in the evolution of the fractured zone. In this context, the present section describes a coupled THM simulation of the ALC1604 in situ heating test but using the thermal extension of the reference model, described in the earlier section 'Thermomechanical constitutive model', to characterise the behaviour of the COx claystone.

Main features of the numerical model

A THM 2D finite-element (FE) analysis of the in situ heating tests was performed assuming plane-strain

Table 1. Model parameters adopted for the simulation of the triaxial tests from Menaceur *et al.* (2015) and the lateral decompression tests from Liu *et al.* (2019) with temperature control

Parameter	Units	Triaxial	Decompression
E	MPa	2000	6000
v	–	0·1	0·1
$\phi_{\text{ini}}^{T_0}$	degrees	9·35	9·35
$\phi_{\text{peak}}^{T_0}$	degrees	21·0	21·0
$\phi_{\text{res}}^{T_0}$	degrees	11·74	11·74
$c_{\text{peak}}^{T_0}$	MPa	3·5	3·5
a_{hard}	–	0·0035	0·0035
a_{soft}	–	0·07	0·07
ω	–	1·0	1·0
ξ_1	–	0·005	0·005
ξ_2	–	0·006	0·006
ξ_3	–	0·045	0·045
μ_ϕ	–	0·14	0·14
μ_E	–	0·275	0·07

conditions. Details of the adopted coupled THM numerical formulation are given in Olivella *et al.* (1994). The same features and parameters as the 2D model reported in Tourchi *et al.* (2019a, 2019b, 2021) were adopted here, which corresponds to a cross-section located 17·5 m into the tunnel at the centre of heater 3. However, in contrast with the mentioned work, the host rock is characterised now by the thermomechanical extension of the reference model, described in the earlier section 'Thermomechanical constitutive model'. Only a brief description of the FE model is provided here. Further details can be found in Tourchi *et al.* (2021).
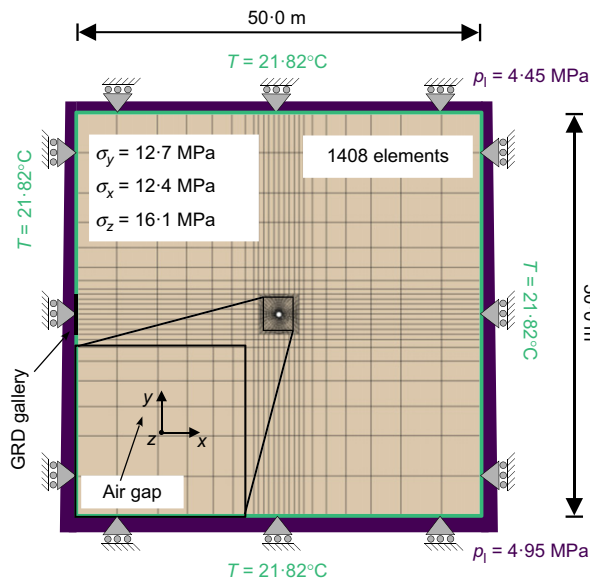
Fig. 7. Model geometry, boundary conditions and finite element mesh employed (Tourchi, 2020)

The model geometry and main boundary conditions are depicted in Fig. 7. The dimensions of the model are 50×50 m, and the 25 m from the microtunnel axis to the lateral boundary corresponds to the distance to the gallery of the GRD tunnel (see Fig. 8). The mesh comprises 1408 quadrilateral elements and 1425 nodes, and it has been refined near the excavation in order to deal with the high temperature and pore pressure gradients in that zone. Null displacements were prescribed in the normal direction of all boundaries. A homogeneous anisotropic initial stress state was considered in the whole domain (i.e. the gravity gradient was neglected), corresponding to the stresses determined at the main level of the MHM URL (-490 m) (Wileveau *et al.*, 2007). An initial hydrostatic pore-water pressure distribution was assumed and prescribed as a boundary condition, which results in a value of 4·7 MPa at the tunnel axis. This value corresponds to the one estimated at this elevation when unaffected by excavation works (Armand *et al.*, 2013, 2014). Regarding thermal conditions, an initial temperature of 21·8°C has been assumed throughout the geometry, and it has been prescribed in all boundaries except at the location of the GRD gallery. Although it was not explicitly included in the simulation, the observed variations of temperature and pore pressures in the gallery were prescribed as boundary conditions at this location. The excavation diameter is 0·7 m, whereas the diameter of the casing is smaller, 0·62 m. The heater rests on the excavation floor, resulting in an annular space of varying thickness between the casing and the COx, which will eventually be closed due to the convergence of the rock. Both the casing and the annular space were explicitly included in the simulation (Fig. 7); the former was characterised by a linear elastic material and the latter by a bilinear elastic material, accounting for the gap closure. More details can be consulted in Tourchi *et al.* (2021). At the excavation boundary, a liquid pressure of 0·1 MPa (atmospheric) was prescribed after excavation. Heat power was applied as a thermal flux on the microtunnel. Ninety per cent of the heat power was applied uniformly in the zone of the
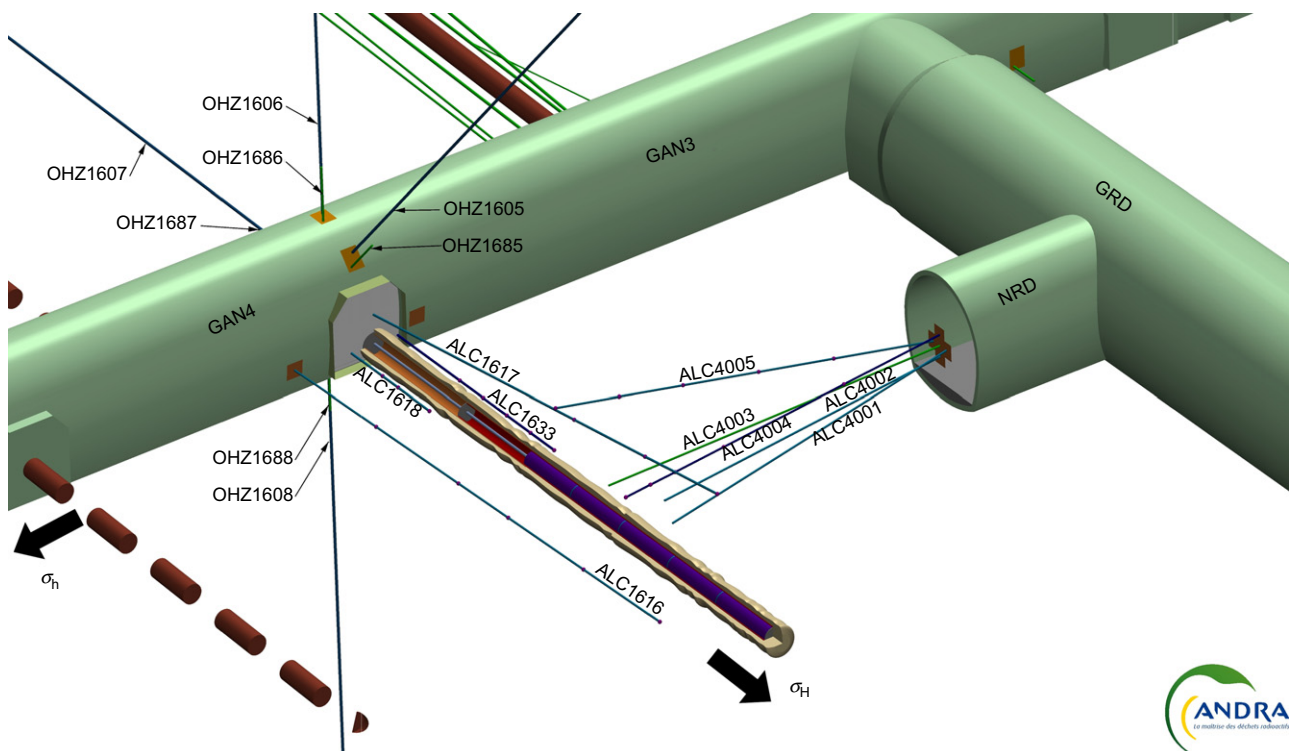

Fig. 8. Schematic layout of the ALC1604 in situ heating tests (Bumbieler *et al.*, 2021).

Table 2. Stages of ALC1604 in situ test

Phase	Description	Start date	End date	Duration
1	Galleries GAN-GRD excavation	9 September 2010	23 October 2012	775 days
2	Alveoli excavation	23 October 2012	31 October 2012	8 days
3	Boreholes/Instrumentation	31 October 2012	30 January 2013	91 days
4	Heating test (30 W/m)	30 January 2013	15 February 2013	16 days
5	Cooling	15 February 2013	18 April 2013	62 days
6	Heating stage (220 W/m)	18 April 2013	6 February 2019	2120 days
7	First cooling phase (200 W/m)	6 February 2019	8 April 2019	61 days
8	Second cooling phase (167 W/m)	8 April 2019	11 June 2019	64 days

heaters, while the remaining 10% was applied in the air-filled annular space between the heater and the lining in order to approximately reproduce the effects of radiation and air thermal convection. The partition of the total heat flux was calibrated based on the temperature observations. Details on different stages of the experiment are given in Table 2.

A number of boreholes were drilled from the galleries of the GAN and NRD tunnels (Fig. 8), where several measurement devices were installed, including temperature sensors and piezometers. Fig. 9 shows the location of the observation points contained in the analysis section, which are used for comparison with the simulation results.

Tables 3 and 4 show the parameters adopted for the COx claystone, relevant for the coupled THM simulation performed. All parameters correspond to those employed in Tourchi *et al.* (2021), except for μ_ϕ and μ_E, controlling the evolution of the strength and the stiffness with temperature, selected based on the simulation of the non-isothermal tests on COx samples described in the section on 'Model validation'. The parameters employed for the casing and the annular space are shown in Tables 5 and 6, respectively, which also coincide with those adopted in Tourchi *et al.* (2021).

Results of the analysis

Figure 10 shows the resulting temperature field at the end of heating. A maximum temperature of about 85°C was reached in the vicinity of the excavation. The anisotropic response of the heat flux is evident in the temperature field, extending somewhat more in the horizontal than in the vertical direction. The latter is the result of the assumed higher thermal conductivity parallel to bedding, compared to the value normal to bedding (Gens *et al.*, 2007). Fig. 11 shows the observed and computed evolution of temperature at the sensors indicated in Fig. 9. The figure also shows the results obtained by Tourchi *et al.* (2021), using the isothermal version of the reference model. Although, in general, the results satisfactorily reproduced the observed behaviour, the importance of the heat dissipation in the direction normal to the analysis section has already been demonstrated by Tourchi *et al.* (2021), and better results can be obtained with a 3D analysis. Nevertheless, it is important to notice that quite similar results are obtained with the isothermal and non-isothermal versions of the reference model. The latter can be attributed to the fact that the hydraulic and mechanical responses of the claystone do not significantly affect the thermal behaviour (Gens *et al.*, 2007).

The resulting fractured zone (*a*) at the end of the excavation and (*b*) at the end of the heating phase is shown in Fig. 12 in terms of the cumulative value of the plastic multiplier, which is directly related to the magnitude of irreversible plastic strains and, therefore, is related to the degree of damage experienced by the host rock surrounding the excavation. The drift for the ALC1604 experiment is
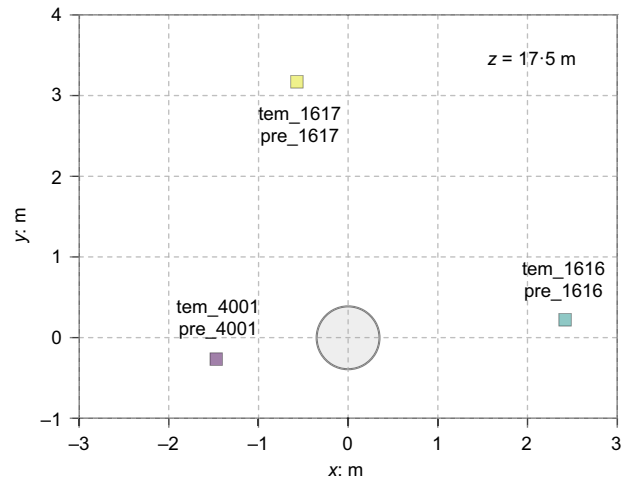
Fig. 9. Location of the temperature and pore-water pressure measurement sensors used for comparison with simulation results

Table 3. COx properties used in the simulation (modified from Tourchi *et al.* (2021))

Parameter	Value
Hydraulic	
Horizontal intrinsic permeability of the intact rock, $k_{0,xx}$: m²	$2\cdot0 \times 10^{-20}$
Vertical intrinsic permeability of the intact rock, $k_{0,yy}$: m²	$1\cdot0 \times 10^{-20}$
Parameter for the increase of k_0, η	300
Parameter for the increase of k_0, λ_{thr}	$1\cdot2 \times 10^{-4}$
Parameter in retention curve model, P: MPa	14·3
Parameter in retention curve model, λ_r	0·33
Parameter in the relative permeability model, A	1·0
Parameter in the relative permeability model, Λ	3·0
Hydro-mechanical	
Biot coefficient, B	0·6
Thermal	
Horizontal thermal conductivity, $k_{T,xx}$: (W/m)/K	2·05
Vertical thermal conductivity, $k_{T,yy}$: (W/m)/K	1·33
Specific heat capacity of the solid, c_s: (J/kg)/K	800
Thermomechanical	
Linear thermal expansion coefficient of solids, α_s: K⁻¹	$1\cdot4 \times 10^{-5}$
Petrophysical	
Solid compressibility, β_s: MPa⁻¹	$2\cdot5 \times 10^{-5}$
Relative density, ρ_s	2·7
Porosity, Φ	0·173

aligned parallel to the major horizontal stress σ_H and, therefore, there is a nearly isotropic initial stress state in planes normal to the tunnel axis (see Fig. 7). However, the

Table 4. COx mechanical parameters for the thermomechanical reference model (modified from Tourchi et al. (2021))

Parameter	Value
Young's modulus, E_1: MPa	5200
Young's modulus, E_2: MPa	4000
Shear modulus, G_2: MPa	1480
Poisson's ratio, v_1	0·25
Poisson's ratio, v_2	0·35
Initial friction angle, $\phi_{ini}^{T_0}$: degrees	9·35
Peak friction angle, $\phi_{peak}^{T_0}$: degrees	22·0
Residual friction angle, $\phi_{residual}^{T_0}$: degrees	14·74
Peak cohesion, $c_{peak}^{T_0}$: MPa	3·55
Parameter controlling hardening, a_{hard}	0·0035
Parameter controlling softening, a_{soft}	0·07
Parameter in the flow rule, ω	0·60
Value of ε_{eq}^{p} at peak strength, ξ_1	0·005
Value of ε_{eq}^{p} at residual strength, ξ_3	0·006
Threshold for viscoplastic strains, σ_s: MPa	4·0
Viscosity parameters, γ: day^{-1}	$1·0 \times 10^{-7}$
Parameter in the time-dependent component, n	3·37
Parameter in the time-dependent component, m	530
Normal scaling factor for anisotropy, C_N	1·33
Shear scaling factor for anisotropy, C_S	1·0
Rate of reduction of the stiffness with temperature, μ_E	0·27
Rate of reduction of the strength with temperature, μ_ϕ	0·14

Table 5. Parameters adopted for the steel casing (modified from Tourchi et al. (2021))

Parameter	Value
Mechanical	
Young's modulus, E: GPa	210·0
Poisson's ratio, v	0·3
Thermal	
Thermal conductivity, k_T: (W/m)/K	80
Specific heat capacity, c_s: (J/kg)/K	550
Linear thermal expansion coefficient of solids, α_s: K^{-1}	$1·4 \times 10^{-5}$

Table 6. Parameters adopted for the annular space (modified from Tourchi et al. (2021))

Parameter	Value
Mechanical	
Young's modulus, E_{open}: MPa	10·0
Young's modulus, E_{closed}: MPa	1000·0
Poisson's ratio, v	0·3
Volumetric strain for gap closure, $\varepsilon_{v,limit}$	0·005–0·21
Thermal	
Thermal conductivity, $k_{T,dry}$: (W/m)/K	0·035
Thermal conductivity, $k_{T,sat}$: (W/m)/K	0·6
Hydraulic	
Intrinsic permeability, k: m^2	$1·0 \times 10^{-16}$
Parameter in retention curve model, P: MPa	0·001
Parameter in retention curve model, λ_r	0·5

fractured zone extends further in the horizontal direction for tunnels with this orientation (Armand et al., 2014), owing to the anisotropic characteristics of the rock mass. This behaviour can be reproduced by including strength anisotropy in the constitutive description (Mánica et al., 2016, 2017, 2022a, 2022b), as done in the reference model (see earlier section 'Isothermal reference model (Mánica et al., 2017)').
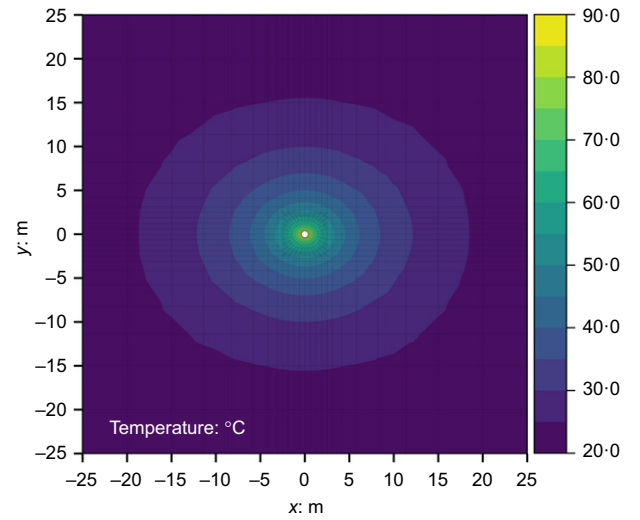
Fig. 10. Computed contours of temperature for the end of heating
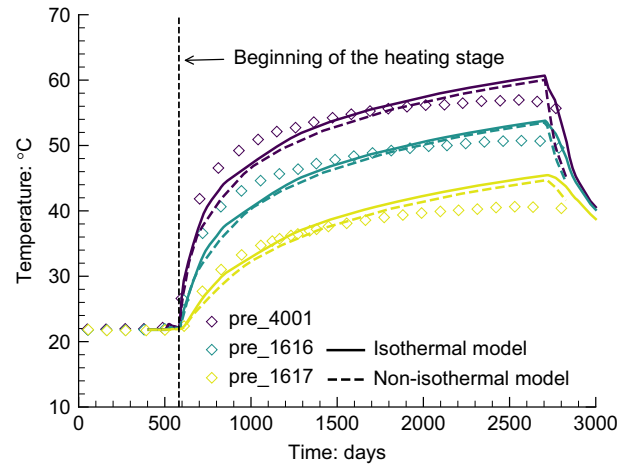
Fig. 11. Observed and computed evolution of temperature at the observation points shown in Fig. 9. A full-colour version of this figure can be found on the ICE Virtual Library (www.icevirtuallibrary.com)

Therefore, the resulting contours of the plastic multiplier nicely resemble the observed configuration of the fractured zone for tunnels with this orientation. The same satisfactory results were obtained by Tourchi et al. (2021), using the isothermal version of the model. However, in contrast to what is reported by Tourchi et al. (2021), the fractured zone shows a significant evolution during the heating stage (Fig. 12(b)). The latter can be more easily identified in Fig. 13, showing the resulting cumulative value of the plastic multiplier, along a horizontal line from the tunnel wall, for the simulations using the isothermal and non-isothermal versions of the reference model; the simulation with the non-isothermal model results in a larger size of the fractured zone. This occurs because as temperature increases, the strength and stiffness of the material decrease, generating additional damage and the accumulation of plastic deformations.

To the best knowledge of the authors, there were no direct in situ measurements to assess the evolution of the fractured zone after heating to validate the results obtained from the analysis. However, as demonstrated by Mánica et al. (2022a, 2022b), the fractured zone plays a major role in the behaviour of pore-water pressures in the host rock. In particular, the increase of permeability due to damage significantly modifies
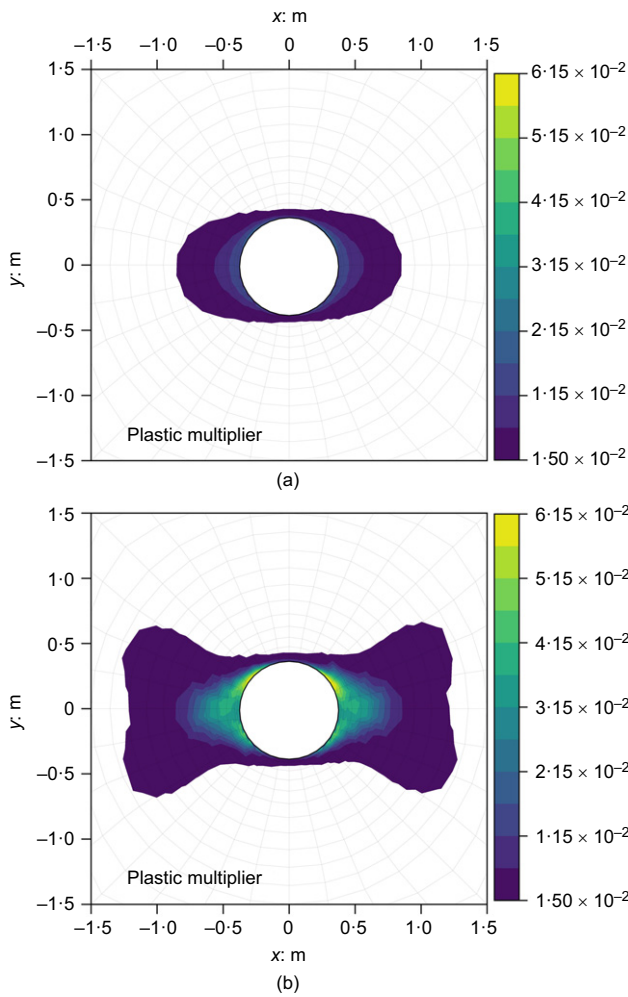
Fig. 12. Obtained configuration of the fractured zone in terms of contours of the plastic multiplier (a) after excavation and (b) at the end of the heating phase
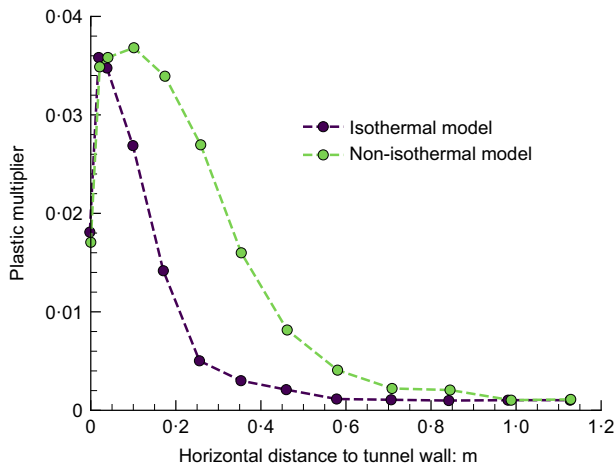

Fig. 13. Computed plastic multiplier at the end of heating in the horizontal direction
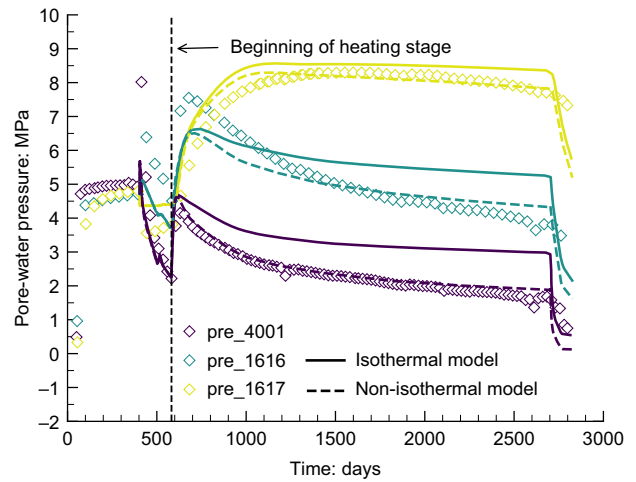

Fig. 14. Computed pore-water pressure evolution at the observation points indicated in Fig. 9

with the horizontal direction (pre_1616 and pre_4001), there is an increase of the pressure as the excavation front approaches the analyses section, while in the vertical direction (pre_1617) the pressure is reduced. The latter is the result of the anisotropic deconfinement brought about by the anisotropic stiffness of the COx (see Mánica *et al*. (2022a) for further details). After the excavation front reaches the analysis section, the pressure at pre_1616 and pre_4001 drops rapidly due to the pressure gradient generated by the new hydraulic boundary condition, enhanced by the permeability increase due to damage. However, when heating begins, the pressure increases sharply due to the thermal pressurisation of water caused by the differential thermal expansion of the liquid and solid phases. Nevertheless, consolidation (i.e. the dissipation of excess pore-water pressures) occurs simultaneously, acting as a competing phenomenon. When the rate of increase of temperature decreases (see Fig. 11), as the temperature field approaches steady-state conditions, consolidation starts to dominate, causing the reduction of pore pressures. In general, both simulations, with the isothermal and non-isothermal models, reasonably capture the evolution of water pressures during the experiment. Nevertheless, results with the non-isothermal model are significantly closer to field values when consolidation dominates the pore-water pressure behaviour. The latter is the result of a larger extension of the fractured zone (see Fig. 13), causing the permeability increase with damage (equation (20)) to occur further into the claystone, resulting in lower pressures that are more consistent with field values. These observations suggest that the evolution of mechanical parameters with temperature might result in some limited enlargement of the fractured zone during heating.

CONCLUDING REMARKS

This paper presents the enhancement of an existing constitutive model for the coupled THM simulation of deep excavations in argillaceous rocks subjected to thermal loading. The original model includes a number of features that are relevant for the satisfactory description of these indurated clayey materials, such as strength and stiffness anisotropy, non-linear isotropic hardening/softening, time-dependent deformations and the evolution of permeability with damage. The non-isothermal extension is obtained by accounting for the observed evolution of mechanical (strength and stiffness) parameters with temperature. The model focuses on the deviatoric yielding mechanism, which

the steady-state pore-water pressure distribution. Therefore, the behaviour of pore pressures can be employed to indirectly assess the computed evolution of the fractured zone with the non-isothermal model.

Figure 14 shows the pore-water pressures at the locations indicated in Fig. 9. In the piezometers approximately aligned

is characterised by a Mohr–Coulomb criterion. Therefore, the effect of temperature on the strength is incorporated through the evolution of the friction angle and the cohesion with temperature.

The resulting thermomechanical model has been validated through the simulation of relevant non-isothermal laboratory tests on COx argillite from the literature. The model was then applied to the 2D simulation of an in situ heating test at the MHM URL. Results were compared to in situ measurements and to the results obtained in previous simulations using the isothermal version of the model (Tourchi *et al.*, 2021). It is shown that both the isothermal and non-isothermal versions reproduce satisfactorily the main trends of behaviour in terms of the configuration and extension of the fractured zone, and the evolution of temperature and pore-water pressure around the excavation, in the host rock. However, the non-isothermal model results in a larger evolution of the fractured zone during the heating phase of the experiment. This results in a larger zone where the permeability increases due to damage taking place and, therefore, in lower water pressures that are more consistent with field values. These results show that the incorporation of thermal effects into the constitutive description of the host rocks plays a significant role in the behaviour of the excavation when subjected to thermal loading.

ACKNOWLEDGEMENTS

NOTATION

A	parameter in the relative permeability model
a_{hard}	parameter in the hardening/softening law
a_{soft}	parameter in the hardening/softening law
B	Biot's coefficient
c	cohesion
c_{mob}	mobilised cohesion
$c_{mob}(T)$	temperature-dependent mobilised cohesion
c_N	normal scaling factor
c_{peak}	peak cohesion
$c_{peak}^{T_0}$	peak cohesion at reference temperature
c_S	shear scaling factor
c_s	specific heat capacity
E	Young's modulus
$E(T)$	temperature-dependent Young's modulus
$E(T_0)$	Young's modulus at reference temperature
E_1	Young's modulus parallel to the isotropic plane
E_2	Young's modulus normal to the isotropic plane
E_{closed}	Young's modulus for the annular space (closed)
E_{open}	Young's modulus for the annular space (opened)
G_2	shear modulus in planes normal to the isotropic plane
g	plastic potential function
$\boldsymbol{I}$	identity tensor
J	deviatoric stress invariant
J^{ani}	anisotropic deviatoric stress invariant
$\boldsymbol{k}$	intrinsic permeability tensor of the fractured rock
k	intrinsic permeability
$\boldsymbol{k}_0$	intrinsic permeability tensor of the intact rock
$k_{0,xx}$	horizontal intrinsic permeability of the intact rock
$k_{0,yy}$	vertical intrinsic permeability of the intact rock
k_T	thermal conductivity
$k_{T,dry}$	thermal conductivity for dry conditions
$k_{T,sat}$	thermal conductivity for saturated conditions
$k_{T,xx}$	horizontal thermal conductivity
$k_{T,yy}$	vertical thermal conductivity
m	parameter in the time-dependent component
n	parameter in the time-dependent component

P	parameter in the retention curve model
p	mean stress
p^{ani}	anisotropic mean stress
p_g	gas pressure
p_l	liquid pressure
q_{peak}	peak deviatoric stress
$q_{peak}(T)$	temperature-dependent peak deviatoric stress
$q_{peak}(T_0)$	peak deviatoric stress at reference temperature
S_e	effective degree of saturation
S_l	degree of saturation
S_{lr}	residual degree of saturation
S_{ls}	degree of saturation in saturated conditions
$\boldsymbol{s}$	deviatoric stress tensor
s	suction
T	temperature
T_0	reference temperature
t	time
α_s	linear thermal expansion coefficient of solids
β_s	solid compressibility
γ	viscosity parameter
ε	total strain tensor
ε^e	elastic strain tensor
$\boldsymbol{\varepsilon}^{ep}$	elastoplastic strain tensor
$\boldsymbol{\varepsilon}^{e,\sigma}$	elastic strain tensor due to changes of effective stresses
$\boldsymbol{\varepsilon}^p$	plastic strain tensor
$\boldsymbol{\varepsilon}^{vp}$	viscoplastic strain tensor
$\dot{\boldsymbol{\varepsilon}}^{vp}$	viscoplastic strain rate tensor
$\varepsilon_v^{e,T}$	volumetric elastic strains due to changes in temperature
$\varepsilon_{v,limit}$	volumetric strain for gap closure
ε_{eq}^p	equivalent plastic strain
ε_{eq}^{vp}	equivalent viscoplastic strain
$\dot{\varepsilon}^{vp}$	viscoplastic strain rate
η	parameter for the increase of k_0
θ	Lode angle
θ^{ani}	anisotropic lode angle
Λ	parameter in the relative permeability model
λ	plastic multiplier
λ_r	parameter in the retention curve model
λ_{thr}	parameter for the increase of k_0
μ_E	parameter controlling the rate of reduction of E with temperature
μ_q	parameter controlling the rate of reduction of q with temperature
μ_ϕ	parameter controlling the rate of reduction of ϕ with temperature
v_1	Poisson's ratio for the lateral strains due to loading parallel to the isotropic plane
v_2	Poisson's ratio for the lateral strains due to loading normal to the isotropic plane
ξ_1	value of ε_{eq}^p at peak strength
ξ_2	value of ε_{eq}^p at which softening begins
ξ_3	value of ε_{eq}^p at the residual strength
ρ_s	relative density
$\boldsymbol{\sigma}$	stress tensor
$\boldsymbol{\sigma}'$	effective stress tensor
$\boldsymbol{\sigma}^{ani}$	anisotropic stress tensor
$\boldsymbol{\sigma}^r$	stress tensor oriented with respect to bedding orientation
σ_H	major horizontal stress
σ_{ii}^r	stress components of $\boldsymbol{\sigma}^r$
σ_s	threshold stress from which viscoplastic strains are activated
Φ	porosity
ϕ	friction angle
ϕ_{ini}	initial friction angle
$\phi_{ini}(T)$	temperature-dependent initial friction angle
$\phi_{ini}^{T_0}$	initial friction angle at reference temperature
ϕ_{mob}	mobilised friction angle
ϕ_{peak}	peak friction angle
$\phi_{peak}(T)$	temperature-dependent peak friction angle
$\phi_{peak}^{T_0}$	peak friction angle at reference temperature
ϕ_{res}	residual friction angle
$\phi_{res}(T)$	temperature-dependent residual friction angle
$\phi_{res}^{T_0}$	residual friction angle at reference temperature
ω	parameter in the plastic potential function controlling the rate of volumetric plastic strains
$\langle \cdot \rangle$	Macaulay brackets

REFERENCES

Abuel-Naga, H. M., Bergado, D. T., Ramana, G. V., Grino, L., Rujivipat, P. & Thet, Y. (2006). Experimental evaluation of engineering behavior of soft Bangkok clay under elevated temperature. *J. Geotech. Geoenviron. Engng* **132**, No. 7, 902–910, https://doi.org/10.1061/(asce)1090-0241(2006)132:7 (902).

Abuel-Naga, H. M., Bergado, D. T., Bouazza, A. & Pender, M. (2009). Thermomechanical model for saturated clays. *Géotechnique* **59**, No. 3, 273–278, https://doi.org/10.1680/geot. 2009.59.3.273.

Alonso, M., Vu, M. N., Vaunat, J., Armand, G., Gens, A., Plua, C., De Lesquen, C. & Ozanam, O. (2021). Effect of thermo-hydro-mechanical coupling on the evolution of stress in the concrete liner of an underground drift in the Cigéo project. *IOP Conf. Ser.: Earth Environ. Sci.* **833**, 1–8, https://doi.org/ 10.1088/1755-1315/833/1/012200.

Armand, G., Noiret, A., Zghondi, J. & Seyedi, D. M. (2013). Short- and long-term behaviors of drifts in the Callovo-Oxfordian claystone at the Meuse/Haute-Marne Underground Research Laboratory. *J. Rock Mech. Geotech. Engng* **5**, No. 3, 221–230, https://doi.org/10.1016/j.jrmge.2013.05.005.

Armand, G., Leveau, F., Nussbaum, C., de La Vaissiere, R., Noiret, A., Jaeggi, D., Landrein, P. & Righini, C. (2014). Geometry and properties of the excavation-induced fractures at the Meuse/Haute-Marne URL drifts. *Rock Mech. Rock Engng* **47**, No. 1, 21–41, https://doi.org/10.1007/s00603-012-0339-6.

Armand, G., Conil, N., Talandier, J. & Seyedi, D. M. (2017). Fundamental aspects of the hydromechanical behaviour of Callovo-Oxfordian claystone: from experimental studies to model calibration and validation. *Comput. Geotech.* **85**, 277–286, https://doi.org/10.1016/j.compgeo.2016.06.003.

Baldi, G., Hueckel, T. & Pellegrini, R. (1988). Thermal volume changes of the mineral–water system in low-porosity clay soils. *Can. Geotech. J.* **25**, No. 4, 807–825, https://doi.org/10.1139/ t88-089.

Belmokhtar, M., Delage, P., Ghabezloo, S. & Conil, N. (2017). Thermal volume changes and creep in the Callovo-Oxfordian claystone. *Rock Mech. Rock Engng* **50**, No. 9, 2297–2309, https://doi.org/10.1007/s00603-017-1238-7.

Bumbieler, F., Plúa, C., Tourchi, S., Vu, M. N., Vaunat, J., Gens, A. & Armand, G. (2021). Feasibility of constructing a full-scale radioactive high-level waste disposal cell and characterization of its thermo-hydro-mechanical behavior. *Int. J. Rock Mech. Min. Sci.* **137**, 104555, https://doi.org/10.1016/j.ijrmms.2020.104555.

Campanella, R. G. & Mitchell, J. K. (1968). Influence of temperature variations on soil behavior. *J. Soil Mech. Found. Div.* **94**, No. 3, 709–734, https://doi.org/10.1061/JSFEAQ. 0001136.

Cekerevac, C. & Laloui, L. (2004). Experimental study of thermal effects on the mechanical behaviour of a clay. *Int. J. Numer. Analyt. Methods Geomech.* **28**, No. 3, 209–228, https://doi. org/10.1002/nag.332.

Chaboche, J. L. (2008). A review of some plasticity and viscoplasticity constitutive theories. *Int. J. Plast.* **24**, No. 10, 1642–1693, https://doi.org/10.1016/j.ijplas.2008.03.009.

Cheng, W., Peng Chen, R., Yun Hong, P., Jun Cui, Y. & Pereira, J. M. (2020). A two-surface thermomechanical plasticity model considering thermal cyclic behavior. *Acta Geotech.* **15**, No. 10, 2741–2755, https://doi.org/10.1007/s11440-020-00999-5.

Cui, Y. J., Sultan, N. & Delage, P. (2000). A thermomechanical model for saturated clays. *Can. Geotech. J.* **37**, No. 3, 607–620, https://doi.org/10.1139/t99-111.

De Bruyn, D. & Thimus, J. F. (1996). The influence of temperature on mechanical characteristics of Boom clay: the results of an initial laboratory programme. *Engng Geol.* **41**, No. 1–4, 117–126, https://doi.org/10.1016/0013-7952(95)00029-1.

Di Donna, A. & Laloui, L. (2015). Response of soil subjected to thermal cyclic loading: experimental and constitutive study. *Engng Geol.* **190**, 65–76, https://doi.org/10.1016/j.enggeo.2015. 03.003.

Gens, A. (2013). On the hydromechanical behaviour of argillaceous hard soils-weak rocks. In *Proceedings of the 15th European conference on soil mechanics and geotechnical engineering – geotechnics of hard soils–weak rocks* (eds A. Anagnostopoulos,

M. Pachakis and C. Tsatsanifos), vol. 4, pp. 71–118, https://doi. org/10.3233/978-1-61499-199-1-71. Amsterdam, the Netherlands: IOS Press.

Gens, A., Vaunat, J., Garitte, B. & Wileveau, Y. (2007). In situ behaviour of a stiff layered clay subject to thermal loading: observations and interpretation. *Géotechnique* **57**, No. 2, 207–228, https://doi.org/10.1680/geot.2007.57.2.207.

Gens, A., Manica, M., Vaunat, J. & Ruiz, D. F. (2017). Modelling the mechanical behaviour of Callovo-Oxfordian argillite. Formulation and application. In *Advances in laboratory testing and modelling of soils and shales (ATMSS)* (eds A. Ferrari and L. Laloui), pp. 37–44, https://doi.org/10.1007/978-3-319-52773-4. Berlin, Germany: Springer.

Golchin, A., Vardon, P. J. & Hicks, M. A. (2022). A thermo-dynamically consistent two surface/bubble thermo-mechanical model considering thermal and mechanical cyclic behaviour of fine-grained soils. *Int. J. Solids Structs* **254–255**, 111847, https://doi.org/10.1016/j.ijsolstr.2022.111847.

Graham, J., Tanaka, N., Crilly, T. & Alfaro, M. (2001). Modified Cam-Clay modelling of temperature effects in clays. *Can. Geotech. J.* **38**, No. 3, 608–621, https://doi.org/10.1139/ t00-125.

Hamidi, A. & Tourchi, S. (2018). A thermomechanical constitutive model for unsaturated clays. *Int. J. Geotech. Engng* **12**, No. 2, 185–199, https://doi.org/10.1080/19386362.2016.1260312.

Hamidi, A., Tourchi, S. & Khazaei, C. (2015). Thermomechanical constitutive model for saturated clays based on critical state theory. *Int. J. Geomech.* **15**, No. 1, 4014038, https://doi.org/ 10.1061/(ASCE)GM.1943-5622.0000402.

Hamidi, A., Tourchi, S. & Kardooni, F. (2017). A critical state based thermo-elasto-plastic constitutive model for structured clays. *J. Rock Mech. Geotech. Engng* **9**, No. 6, 1094–1103, https://doi. org/10.1016/j.jrmge.2017.09.002.

Hueckel, T. & Borsetto, M. (1990). Thermoplasticity of saturated soils and shales: constitutive equations. *J. Geotech. Engng* **116**, No. 12, 1765–1777, https://doi.org/10.1061/(ASCE)0733-9410 (1990)116:12(1765).

Laloui, L. & Cekerevac, C. (2008). Non-isothermal plasticity model for cyclic behaviour of soils. *Int. J. Numer. Analyt. Methods Geomech.* **32**, No. 5, 437–460, https://doi.org/10.1002/nag.629.

Laloui, L. & François, B. (2009). ACMEG-T: soil thermoplasticity model. *J. Engng Mech.* **135**, No. 9, 932–944, https://doi.org/ 10.1061/(ASCE)EM.1943-7889.0000011.

Liu, Z., Shao, J., Xie, S., Conil, N. & Talandier, J. (2019). Mechanical behavior of claystone in lateral decompression test and thermal effect. *Rock Mech. Rock Engng* **52**, No. 2, 321–334, https://doi.org/10.1007/s00603-018-1573-3.

Mánica, M. A., Gens, A., Vaunat, J. & Ruiz, D. F. (2016). A cross-anisotropic formulation for elasto-plastic models. *Géotechnique Lett.* **6**, No. 2, 156–162, https://doi.org/10.1680/ jgele.15.00182.

Mánica, M., Gens, A., Vaunat, J. & Ruiz, D. F. (2017). A time-dependent anisotropic model for argillaceous rocks. Application to an underground excavation in Callovo-Oxfordian claystone. *Comput. Geotech.* **85**, 341–350, https:// doi.org/10.1016/j.compgeo.2016.11.004.

Mánica, M. A., Gens, A., Vaunat, J., Armand, G. & Vu, M. N. (2022a). Numerical simulation of underground excavations in an indurated clay using non-local regularisation. Part 1: formulation and base case. *Géotechnique* **72**, No. 12, 1092–1112, https://doi.org/10.1680/jgeot.20.P.246.

Mánica, M. A., Gens, A., Vaunat, J., Armand, G. & Vu, M. N. (2022b). Numerical simulation of underground excavations in an indurated clay using non-local regularisation. Part 2: sensitivity analysis. *Géotechnique* **72**, No. 12, 1113–1128, https://doi.org/10.1680/jgeot.20.p.247.

Menaceur, H., Delage, P., Tang, A. M. & Conil, N. (2015). The thermo-mechanical behaviour of the Callovo-Oxfordian claystone. *Int. J. Rock Mech. Min. Sci.* **78**, 290–303, https://doi. org/10.1016/j.ijrmms.2015.07.002.

Modaressi, H. & Laloui, L. (1997). A thermo-viscoplastic constitutive model for clays. *Int. J. Numer. Analyt. Methods Geomech.* **21**, No. 5, 313–335, https://doi.org/10.1002/(SICI)1096-9853 (199705)21:5<313::AID-NAG872>3.0.CO;2-5.

Mohajerani, M., Delage, P., Sulem, J., Monfared, M., Tang, A. M. & Gatmiri, B. (2014). The thermal volume changes of the

Callovo-Oxfordian claystone. *Rock Mech. Rock Engng* **47**, No. 1, 131–142, https://doi.org/10.1007/s00603-013-0369-8.

Monfared, M., Sulem, J., Delage, P. & Mohajerani, M. (2012). On the THM behaviour of a sheared Boom clay sample: application to the behaviour and sealing properties of the EDZ. *Engng Geol.* **124**, 47–58, https://doi.org/10.1016/j.enggeo.2011.10.002.

Olivella, S., Carrera, J., Gens, A. & Alonso, E. E. (1994). Non-isothermal multiphase flow of brine and gas through saline media. *Transp. Porous Media* **15**, No. 3, 271–293, https://doi.org/10.1007/BF00613282.

Plum, R. L. & Esrig, M. I. (1969). *Some temperature effects on soil compressibility and pore pressure, Highway Research Board special report*, issue 103. Washington, DC, USA: Transportation Research Board.

Robinet, J. C., Rahbaoui, A., Plas, F. & Lebon, P. (1996). A constitutive thermomechanical model for saturated clays. *Engng Geology* **41**, No. 1–4, 145–169, https://doi.org/10.1016/0013-7952(95)00049-6.

Shetty, R., Singh, D. N. & Ferrari, A. (2019). Volume change characteristics of fine-grained soils due to sequential thermomechanical stresses. *Engng Geol.* **253**, 47–54, https://doi.org/10.1016/j.enggeo.2019.03.008.

Sultan, N., Delage, P. & Cui, Y. J. (2002). Temperature effects on the volume change behaviour of Boom clay. *Engng Geol.* **64**, No. 2–3, 135–145, https://doi.org/10.1016/S0013-7952(01)00143-0.

Tourchi, S. (2020). *THM analysis of argillaceous rocks with application to nuclear waste underground storage.* PhD thesis, Technical University of Catalonia, Barcelona, Spain.

Tourchi, S. & Hamidi, A. (2015). Thermo-mechanical constitutive modeling of unsaturated clays based on the critical state concepts. *J. Rock Mech. Geotech. Engng* **7**, No. 2, 193–198, https://doi.org/10.1016/j.jrmge.2015.02.004.

Tourchi, S., Vaunat, J., Gens, A., Vu, M. N. & Bumbieler, F. (2019a). Coupled THM analysis of long-term anisotropic convergence in the full-scale micro tunnel excavated in the Callovo-Oxfordian argillite. In *VIII International conference on computational methods for coupled problems in science and engineering* (eds E. Oñate, M. Papadrakakis and B. A. Schrefler), pp. 292–299. Sitges, Spain: ECCOMAS.

Tourchi, S., Vaunat, J., Gens, A., Vu, M. N. & Bumbieler, F. (2019b). Thermo-hydro-mechanical simulation of a full-scale steel-lined micro-tunnel excavated in the callovooxfordian claystone. In *XIV International conference on computational plasticity. Fundamentals and applications* (eds E. Onate, D. R. J. Owen, D. Peric and M. Chiumenti), pp. 544–552. Barcelona, Spain: ECCOMAS.

Tourchi, S., Vaunat, J., Gens, A., Bumbieler, F., Vu, M. N. & Armand, G. (2021). A full-scale in situ heating test in Callovo-Oxfordian claystone: observations, analysis and interpretation. *Comput. Geotech.* **133**, 104045, https://doi.org/10.1016/j.compgeo.2021.104045.

Tsutsumi, A. & Tanaka, H. (2012). Combined effects of strain rate and temperature on consolidation behavior of clayey soils. *Soils Found.* **52**, No. 2, 207–215, https://doi.org/10.1016/j.sandf.2012.02.001.

van Genuchten, M. T. (1980). A closed-form equation for predicting the hydraulic conductivity of unsaturated soils. *Soil Sci. Soc. Am. J.* **44**, No. 5, 892–898, https://doi.org/10.2136/sssaj1980.03615995004400050002x.

Wileveau, Y., Cornet, F. H., Desroches, J. & Blumling, P. (2007). Complete in situ stress determination in an argillite sedimentary formation. *Phys. Chem. Earth* **32**, No. 8–14, 866–878, https://doi.org/10.1016/j.pce.2006.03.018.

Wittke, W. (1990). *Rock mechanics: theory and applications with case histories.* Berlin, Germany: Springer-Verlag.

Yao, Y. P. & Zhou, A. N. (2013). Non-isothermal unified hardening model: a thermo-elasto-plastic model for clays. *Géotechnique* **63**, No. 15, 1328–1345, https://doi.org/10.1680/geot.13.P.035.

Zhang, C. L., Rothfuchs, T., Su, K. & Hoteit, N. (2007). Experimental study of the thermo-hydro-mechanical behaviour of indurated clays. *Phys. Chem. Earth* **32**, No. 8–14, 957–965, https://doi.org/10.1016/j.pce.2006.04.038.

Zhang, F., Hu, D. W., Xie, S. Y. & Shao, J. F. (2014). Influences of temperature and water content on mechanical property of argillite. *Eur. J. Environ. Civ. Engng* **18**, No. 2, 173–189, https://doi.org/10.1080/19648189.2013.852485.

Zhang, C. L., Conil, N. & Armand, G. (2017). Thermal effects on clay rocks for deep disposal of high-level radioactive waste. *J. Rock Mech. Geotech. Engng* **9**, No. 3, 463–478, https://doi.org/10.1016/j.jrmge.2016.08.006.

Zhou, C., Fong, K. Y. & Ng, C. W. W. (2017). A new bounding surface model for thermal cyclic behaviour. *Int. J. Numer. Analyt. Methods Geomech.* **41**, No. 16, 1656–1666, https://doi.org/10.1002/nag.2688.